Combustion and Flame 217 (2020) 188–199

Contents lists available at ScienceDirect

Combustion and Flame

journal homepage: www.elsevier.com/locate/combustflame

Drag force for a burning particle

Hancong Zhang[a], Kun Luo[a,*], Nils Erland L. Haugen[b,c], Chaoli Mao[a], Jianren Fan[a]

[a] State Key Laboratory of Clean Energy Utilization, Zhejiang University, Hangzhou 310027, China
[b] SINTEF Energy Research, Trondheim N-7465, Norway
[c] Department of Energy and Process Engineering, Norwegian University of Science and Technology Kolbjørn Hejes vei 1B, Trondheim NO-7491, Norway

ARTICLE INFO

Article history:
Received 1 October 2019
Revised 13 February 2020
Accepted 14 February 2020

Keywords:
Drag force
Particle-resolved simulation
Char particle
Coal combustion
Immersed boundary method

ABSTRACT

Fully-resolved simulations of a burning char particle are performed to understand the effects of chemical reactions on the drag force by using the ghost cell immersed boundary method. The momentum, heat and mass transfers at the interface are all considered. Reactive particle with different reaction rates, temperatures and diameters are simulated and compared with a non-reactive adiabatic particle and a particle with an outflow. The results show that both the heterogeneous reactions and the gaseous reactions increase the drag force, which is converse to the effect observed for a non-reactive particle with a pure outflow. This difference indicates that the species and temperature distributions caused by the chemical reactions around the particle play an important role in shaping the drag force. To consider these effects, the Stefan flow Reynolds number and the non-dimensional gaseous reaction rate are introduced to formulate a new drag force correlation for a burning particle based on the fully-resolved simulations. Good performance of the correlation has been demonstrated in the current conditions, and more evaluation might be required for future work.

1. Introduction

In numerical simulations of multiphase flows, accurate description of the momentum, heat and mass exchanges between the carrier phase and the dispersed phase is essential. Therefore, various models have been developed to close the conservation equations. The interphase momentum exchange is usually described by the drag force coefficient, which is generally regarded as a function of the Reynolds number. Numerous researches have studied the drag force and relevant empirical drag correlations for cold-state flows. For instance, Tritton [1] and Dennis and Chang [2] measured the drag force of a circular cylinder at low and high Reynolds number, respectively, and proposed corresponding drag force correlations. The empirical drag force correlation for a spherical particle was proposed by Clift et al. [3] ($C_D = 24(1 + Re_p^{0.687})/Re_p$) and has been widely used for multiphase flow simulations. Another widely used drag force correlation was put forward by Schiller and Nauman [4]. These drag correlations are of great importance for describing the momentum transfer in dilute cold multiphase flows [5–7].

However, the above drag correlations are influenced by chemical reactions and usually not applicable for reactive multiphase flows. For a reactive particle, one of the difficulties to draw a general drag correlation is that the wall-normal velocity of the particle is often not zero. As a result, the flow Reynolds number is not enough to represent the drag force. The effect of the non-zero wall-normal velocity has been discussed in the previous studies on porous particles and outflow particles. For a porous particle, the fluid phase can penetrate into the particle, leading to a non-zero velocity [40,41]. The governing equation of the flow inside the porous particle follows the Darcy–Brinkman–Forchheimer extended model [8], and the normal component of the velocity at the rear of the surface is called as “base bleed” [9]. According to the studies of Bhattacharyya et al. [10] and Yu et al. [11], the base bleed at the rear of the cylinder has some interaction with the shear layer, making the recirculation wake detach from or penetrate into the cylinder. Therefore, the surface ratio and particle porosity were used to quantify the effect of the porosity in the drag correlation [12].

A particle with outflow has previously been studied as a simplification of an evaporating droplet or a solid fuel particle with a Stefan flow [13], and the outflow velocity condition was implemented at the surface without considering the effect of the species. A number of studies [13–15] show that the outflow tends to reduce the drag force. To take this effect into consideration, a blowing correlation was introduced in the study of Stöllinger et al. [16]. The Stefan flow Reynolds number was also used in the drag correlation [17]. In the study of Higuera [18], a gasification term was added to the drag force calculation besides the pressure and the friction

* Corresponding author.
E-mail address: zjulk@zju.edu.cn (K. Luo).

https://doi.org/10.1016/j.combustflame.2020.02.016
0010-2180/

terms. Interestingly, the recent study of Luo et al. [19] showed that the chemical reactions might increase the drag force of a reactive particle, compared with a an inert particle. Moreover, the properties of the flow in the vicinity of the particle also influence the drag force. Kurose et al. [20] studied the change in drag force due to the sphere being either heated or cooled. It was found that the temperature difference between particles and the inlet flow influenced the drag force, and a heated particle tends to have a larger drag coefficient. The study of Nagata et al. [21] showed that the temperature changes the drag force mainly by altering the kinematic viscosity coefficient in the vicinity of the sphere.

Several recent researches also involved surface reactions of solid fuels [22–24] (e.g. pulverized coal combustion and biomass combustion) and droplet evaporation [25,26]. However, they all focused on the heat and mass transfer properties on the interface, and up to now, the drag force of reactive particle has not yet been well studied. Heterogeneous reactions influence the drag force not only through the Stefan flow. When the momentum, heat and mass transfer occur simultaneously, the drag force of a reactive particle may show a more complex behavior. To explore this phenomenon, particle-resolved simulations of a single burning char particle are performed with the immersed boundary method in the present work. The influence of the heterogeneous and gaseous reactions on the drag force during the process of char combustion is investigated in detail.

The remainder of this paper is structured as follows. The numerical method and simulation setup are described in Section 2. The mechanism of how reactions influence the drag force is discussed in Section 3. The effects of heterogeneous reactions, the gaseous reaction, and the particle temperature are studied, respectively. A new drag force correlation for a burning char particle is also formulated. The last section is devoted to the conclusions.

2. Numerical approach and simulation setup

2.1. Numerical method

Following the study of Luo et al. [19], a high-order finite difference solver [27,28] is improved and used in the present work. The governing equations of gas phase read

$$\frac{D\rho}{Dt} + \rho\nabla\cdot u = 0, \tag{1}$$

$$\frac{Du}{Dt} = \frac{1}{\rho}(-\nabla p + \nabla\cdot(2\rho\nu S)), \tag{2}$$

$$\rho\frac{DY_k}{Dt} = -\nabla\cdot J_k + \dot{\omega}_k, \tag{3}$$

$$\left(c_p - \frac{R}{\overline{W}}\right)\frac{D\ln T}{Dt} = \sum_k \frac{DY_k}{Dt}\left(\frac{R}{W_k} - \frac{h_k}{T}\right) - \frac{R}{\overline{W}}\nabla\cdot u + \frac{2\nu S^2}{T} - \frac{\nabla\cdot q}{\rho T}. \tag{4}$$

In the above set of equations, $D/Dt = \partial/\partial t + u\cdot\nabla$ represents the convective derivative. The traceless rate of train tensor is given by $S_{ij} = \frac{1}{2}(\partial u_i/\partial x_j + \partial u_j/\partial x_i) - \frac{1}{3}\delta_{ij}\nabla\cdot u$, while J is the diffusive flux, and $\dot{\omega}_k$ represents the reaction rate of species k. The reaction rates and the diffusive flux are calculated according to the method mentioned in [28]. Although the energy equation uses $\ln T$ instead of T, it can be easily transformed into the commonly used form by modifying $\frac{D\ln T}{Dt}$ into $\frac{1}{T}\frac{DT}{Dt}$ and using $\frac{Dp}{Dt}$ instead of expanding it based on the equation of state [29]. In the energy equation, the enthalpy is given by h while W is the molar mass of the gas phase and q is the heat flux. The ideal gas equation of state, given by

$$p = \frac{\rho RT}{\overline{W}} \tag{5}$$

is used to close the governing equations.

Because of the heterogeneous reactions at the char particle surface, the velocity, temperature and the species mass fraction at the char surface are affected. It is essential to determine these boundary conditions properly. The mass transfer at the interface is a balance of the convective flux, diffusive flux and heterogeneous reactions, which is given by

$$\bar{n}\cdot\left[\rho Y_k(\bar{V}_k + u_{Stefan})\right] = \dot{m}_k \tag{6}$$

where $\bar{n}$ represents the outward wall-normal unit vector, and $\dot{m}_k$ is the mass production rate of the kth species. The diffusion velocity of the kth species is related to the gradient of the species mass fraction as

$$\bar{V}_k = \frac{1}{X_k\overline{W}}\sum_{j\neq k} W_j D_{k,j}\nabla X_j \tag{7}$$

while u_{Stefan} represents the velocity of the Stefan flow. The total species diffusion flux is zero

$$\sum_k V_k Y_k = 0. \tag{8}$$

Based on mass transfer balance at the surface, the Stefan flow velocity can be formulated as

$$\overline{n}\cdot u_{Stefan} = \frac{1}{\rho}\sum_{k=1}^{K_g}\dot{m}_k\ . \tag{9}$$

The boundary velocity of the particle is a combination of particle shrinking velocity and the Stefan flow velocity, which is given by

$$u_{IB} = u_{Stefan} + v_n = u_{Stefan} + \frac{\int_{surf}\dot{m}_c ds}{s\rho_c}. \tag{10}$$

Here s is the surface area of the particle, and ρ_c is the density of the char particle.

In this study, the temperature gradient within the particle is neglected. Therefore, the heat transfer at the interface contains the diffusive flux, radiation, reaction heat and the heat conduction from the outside of the particle. The particle energy balance is then given by

$$Vc_{p,C}\frac{dT_p}{d\tau} = \int_{surf}\left(-\sigma\varepsilon(T_p^4 - T_0^4) + \sum_{k=1}^{K}\dot{m}_k h_k + \bar{n}\cdot\lambda\nabla T_{gas}\right)ds \tag{11}$$

where V is the volume of the particle, T_0 represents the temperature of the incoming flow, and $c_{p,C}$ is the heat capacity of the char particle. In the radiation term, ε is the emissivity coefficient, and σ is the Stefan–Boltzmann constant. Finally, $\dot{m}_k$and h_k are the reaction rate and enthalpy of species k, respectively. The right hand side (RHS) of the equation is an integral over the particle surface. In addition, the pressure gradient at the surface should be zero because of the no-penetration condition.

The improved ghost cell immersed boundary method [30] can be used to enforce the boundary conditions of velocity, species concentrations, temperature, and pressure. This method is of a second-order accuracy. For more detailed description and validation of the method for char combustion, please refer to the previous research [19].

2.2. Assumptions and simplifications

In this study, a semi-global heterogeneous reaction mechanism of char conversion and a homogeneous reaction of CO oxidation

Table 1
Kinetic Parameters of chemical reactions.

Chemical reaction		B	E (J/mol)	Reference
(R1)	$2C(s) + O_2(g) \rightarrow 2CO(g)$	1.97×10^7	1.98×10^5	Zhang et al. [31]
(R2)	$C(s) + CO_2(g) \rightarrow 2CO(g)$	1.291×10^5	1.91×10^5	Zhang et al. [31]
(R3)	$2CO(g) + O_2(g) \rightarrow 2CO_2(g)$	2.24×10^{12}	1.6742×10^5	Turns [32]

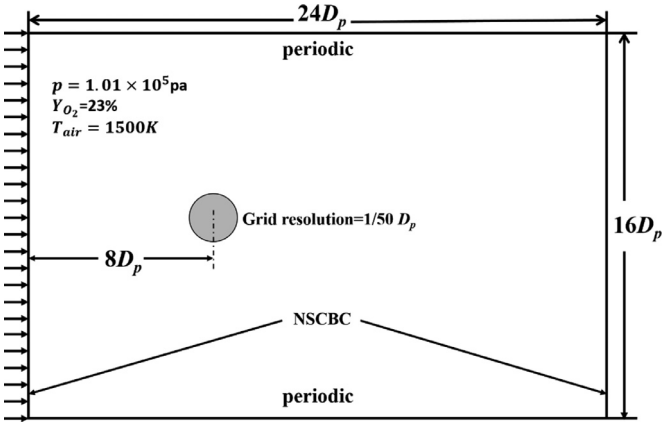

Fig. 1. Schematic of the computational domain.

are used for the simulation. The heterogeneous reactions are essentially from the study of Zhang et al. [31], which have also been validated in our previous study [19]. The kinetic parameters of chemical reactions are shown in Table 1.

Several simplifications and assumptions are made to simplify the task and focus on the key problem. Firstly, the solver we used is fully transient, but it will take too much time to resolve the whole conversion process of the char particle. Therefore, the pseudo-steady-state (PSS) assumption [33] is utilized, according to which we can use the steady condition to represent the transient burning char particle if the characteristic time scales of the convection and diffusion are much shorter than the conversion time scale of the char particle. As a result, the particle temperature and radius can be fixed, and the simulation can reach the quasi-steady state faster. Secondly, the particle is fixed in the flow field and the inlet flow is uniform, which has been a common assumption in many previous studies [34–37]. Thirdly, the gas phase only contains N_2, O_2, CO, and CO_2, and the effect of water gas shift is neglected. The kinematic viscosity is calculated using Wilke's method [38] which considers the effect of species, instead of the Sutherland's temperature dependence viscosity [39].

The drag force on the particle contains two parts, namely the pressure and the friction contributions, as given by the two terms on the RHS in the equation below

$$F_D = \int_A P dA + \int_A \tau dA \ . \tag{12}$$

2.3. Simulation setup

In the simulations, a two-dimensional cylindrical char particle, with diameter D_p, is fixed in the domain. The computational domain has a size of $24D_p \times 16D_p$, and the position of the particle is shown in Fig. 1. The grid resolution is set as $\Delta x = 1/50D_p$. The Navier-Stokes Characteristic Boundary Condition (NSCBC) [45] is used at the inlet and outlet boundaries. Meanwhile, periodic boundary conditions are used in the spanwise direction. Parameters of the incoming flow and the char particle are summarized in Table 2. Different cases of particle Reynolds numbers and particle temperatures are analyzed. Here the particle Reynolds number is

Table 2
Parameters of the simulation conditions.

Parameter	Values
p_0	1.01×10^5 Pa
Y_{O_2}	23% (diluted by N_2)
T_{inlet}	1500 K
Re	5, 10, 20
$T_{particle}$	1400 K, 1500 K, 1600 K, 1800 K
D_p	100 μm, 200 μm, 400 μm
B	$0.1B_0$, $0.5B_0$, $1.0B_0$, $1.5B_0$

given by

$$Re = \frac{UD_p}{\upsilon}. \tag{13}$$

Here, U and υ are the velocity and kinematic viscosity coefficient of the incoming flow. In addition, to analyze the effect of reaction rate, we arbitrarily change the pre-exponential factor (denoted by B *in* Table 2) of the heterogeneous reactions. B_0 refers to the original value of pre-exponential factor of the heterogeneous reactions. At an identical Reynolds number, different diameters cause the variation of the time scale of reactions and diffusion. Therefore, cases with different diameters are also simulated. Each case is simulated until it reaches a quasi-steady state.

3. Results and discussion

3.1. Flow pattern

As mentioned in Section 2.1, the heterogeneous reactions at the surface of the particle result in a Stefan flow, leading to a nonzero normal velocity. This nonzero normal velocity will change the structure of the particle boundary layer. As shown in Fig. 2, when positive wall-normal velocity occurs, the stagnation point at the front of the particle becomes detached from the surface. The position of the stagnation point is farther from the surface when the Stefan flow increases.

The specific separation angle at the surface is hard to be determined because of the Stefan flow. Meanwhile, the recirculation wake structure also changes. According to the simulations of Bhattacharyya et al. [10], the critical Reynolds number of a cylindrical particle when the separation point first occurs is about 7. This criterion is no longer valid for a cylindrical reactive particle. The Stefan flow restrains the formation of the recirculation wake so that the recirculation wake is detached from the particle. The critical Reynolds number where the recirculation wake occurs depends on the Stefan flow at the surface.

To quantify the effect of the Stefan flow, an average Stefan flow Reynolds number over the particle surface is defined and will be discussed in the next section, which is given by

$$Re_{stefan} = \frac{D_p \int_{\text{Surf}} \sum_{k=1}^{K_g} \dot{m}_k ds}{\rho \upsilon}, \tag{14}$$

where ρ and ν are the density and kinematic viscosity coefficient of the incoming flow, and $\dot{m}_k$ is the reaction rate of the kth species on the surface (kg/m^{2}s).

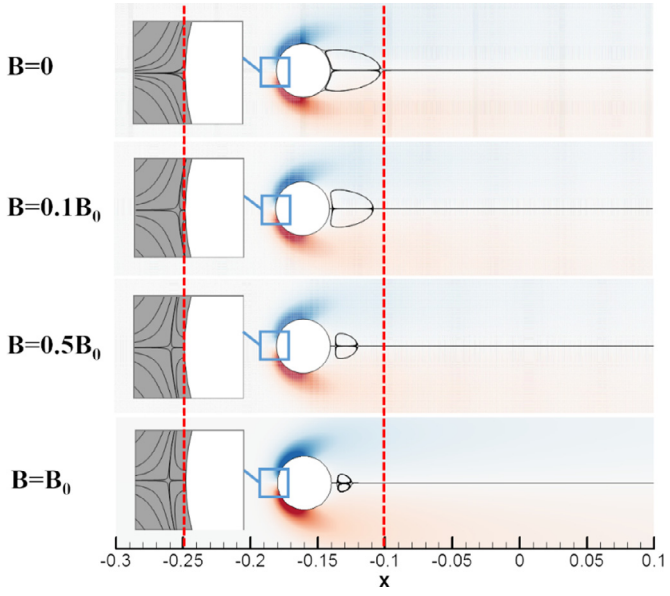

Fig. 2. The vorticity and flow pattern around the particle with different heterogeneous reaction rates ($T_{particle}$ = 1500 K, D_p = 400 μm, Re = 20).

In Fig. 2, the length of the wake becomes shorter and the front of the wake is further from the particle when reaction rates increase. The so-called 'base bleed' of the porous particle has the analogous effect on the recirculation wake [11]. The formation of the recirculating wake can be explained using Leal and Acrivos's entrainment-detrainment mechanism [9]. According to the mechanism, the wake at the rear of the bluff body is formed because the fluid entrained inside the shear layer gets separated from the shear layer and reverses itself again to meet the entrainment need of the shear layer. But for a burning char particle, the wall-normal velocity meets the entrainment demand of shear layer, hence the recirculating wake is weakened.

3.2. Effect of reactions

In the process of char conversion, heterogeneous and gaseous reactions happen simultaneously. Not only the flow pattern is influenced, but also the fluid properties are affected because of the non-uniform temperature and species distribution around the particle. In this section, the effects of heterogeneous and gaseous reactions are analyzed. To simplify the analysis, the particle temperature is set to be equal to the temperature of the incoming flow.

3.2.1. Heterogeneous reactions

In several previous studies, the effects of heterogeneous reactions and evaporation are simplified as a pure outflow [15,42]. Hence, the effect of species distribution resulting from relative rate of reaction and diffusion, is neglected. It was reported that the Stefan flow has little influence on the pressure but attenuates the friction, and thus tends to weaken the drag force [13–15,17]. To investigate whether heterogeneous reactions have the same effect, a comparison of particles with heterogeneous reactions and particles with pure outflow is performed. Fig. 3 shows how the drag, pressure and friction coefficients vary with the Re_{stefan} for a reacting char particle and a non-reacting particle with outflow. For the reacting char particle, the drag force increases slightly with the increasing reaction rate (increasing the Stefan flow). This is in contrast to what is found for the non-reacting particle with an outflow, in which increase in Re_{stefan} results in an obvious decrease in the drag coefficient. At the same Stefan flow Reynolds number, the friction coefficient of the reactive particle is slightly higher than that of the particle with the pure outflow. As a result, the difference in drag force is mainly resultant from the difference in the pressure contribution which is associated with the species profiles caused by the heterogeneous reactions. Hence, it is apparent that a particle with heterogeneous reactions cannot be simplified as just

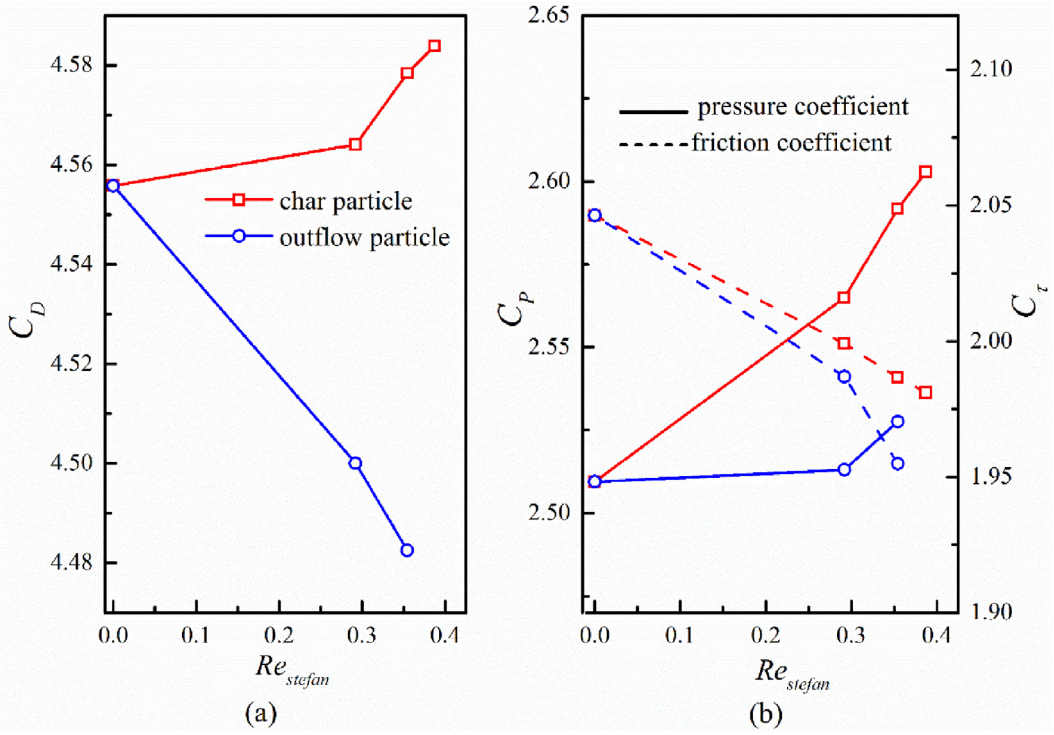

Fig. 3. The comparison of the particle with heterogeneous reactions and the particle with outflow (D_p = 400 μm, Re = 5, $T_{particle}$ = 1500 K for the char particle). (a) Drag force coefficient (b) Pressure and friction coefficients.

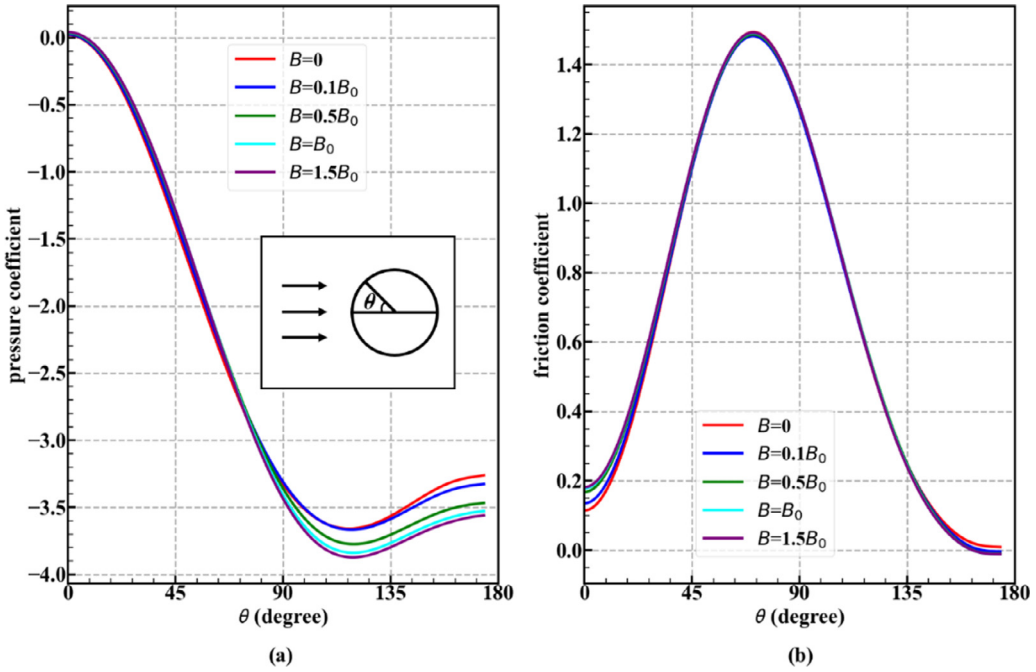

Fig. 4. Local pressure and friction coefficient distribution of particle with different heterogeneous reaction rates ($T_{particle}$ = 1500 K, D_p = 400 μm, Re = 5).

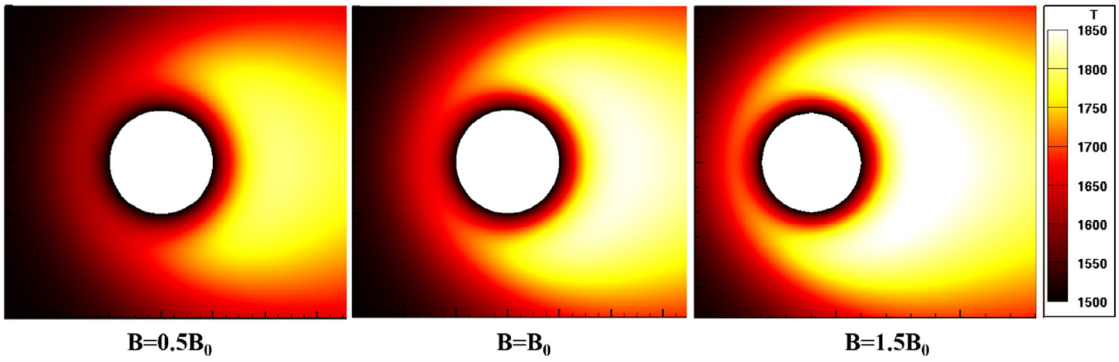

Fig. 5. Temperature contours in the neighborhood of particles with different reaction rates ($T_{particle}$ = 1500 K, D_p = 400 μm, Re = 5).

a particle with an outflow. The drag force of a particle with heterogeneous reactions might be obviously larger than that of a particle with an outflow.

3.2.2. Gaseous reaction

The species distribution and fluid properties are also affected by the gaseous reaction. This effect is little mentioned in previous studies of the particle drag force. According to the above discussion in Section 3.2.1, the effect of species distribution offsets the effect of the outflow on the drag force. Similarly, the gaseous reaction makes this effect more pronounced.

Based on the definition of drag force (as shown in Section 2.2), here we define a local pressure coefficient and a local friction coefficient to describe the distribution of the drag force components;

$$C_{P\_local} = \frac{(p - p_{front})}{1/2\rho U^2},\ C_{\tau\_local} = \frac{\nabla \cdot (2\rho\nu S) \cdot \vec{x}}{1/2\rho U^2} \tag{15}$$

where p_{front} is the pressure at the front point of the cylinder surface in the streamwise direction, and $\vec{x}$ is the streamwise unit vector. The density and the streamwise velocity of the incoming flow are given by ρ and U, respectively. In the following discussions, θ refers to the surface angle of the cylinder, and θ= 0 refers to the front of the cylinder toward the incoming flow.

As the left panel of Fig. 4(a) shows, at the rear of the particle, cases with gaseous reactions have larger pressure drops. According to the ideal gas state equation, the pressure is related to the density, molar mass and temperature of the gas phase, but according to the definition of the pressure coefficient, the density term can be roughly reduced. As a result, the variation of the pressure coefficient is mainly associated with the variation of temperature and the molar mass. Fig. 5 shows that since convection dominates the transport in the vicinity of the particle, CO tends to be consumed at the rear, yielding a high temperature region at a certain distance from the particle. However, the temperature difference between the boundary temperature and the particle temperature is less than 1 K (within 0.067% of the particle temperature) according the simulation results. Considering this negligible difference of temperature, one concludes that the non-uniformity of molar mass plays an important role in the remarkable drop of the pressure coefficient at the rear of the particle. Fig. 6 shows that with the reaction rate increasing, the CO concentration increases at the front of the particle. But because of the gaseous reaction, CO is transformed into CO_2 at the rear region. This change of species profile around the particle finally alter the density and molar mass

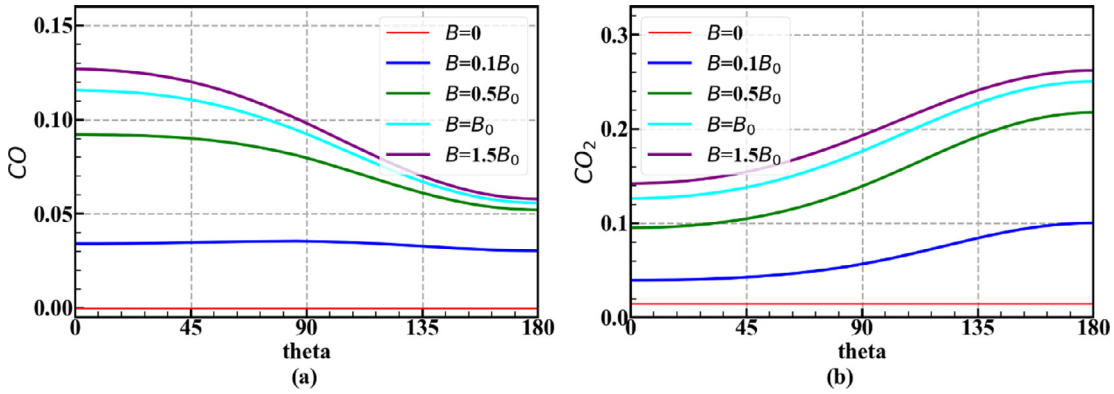

Fig. 6. Y_{CO} and Y_{CO_2} profiles along the particle surface. ($T_{particle}$ = 1500 K, D_p = 400 μm, Re = 5).

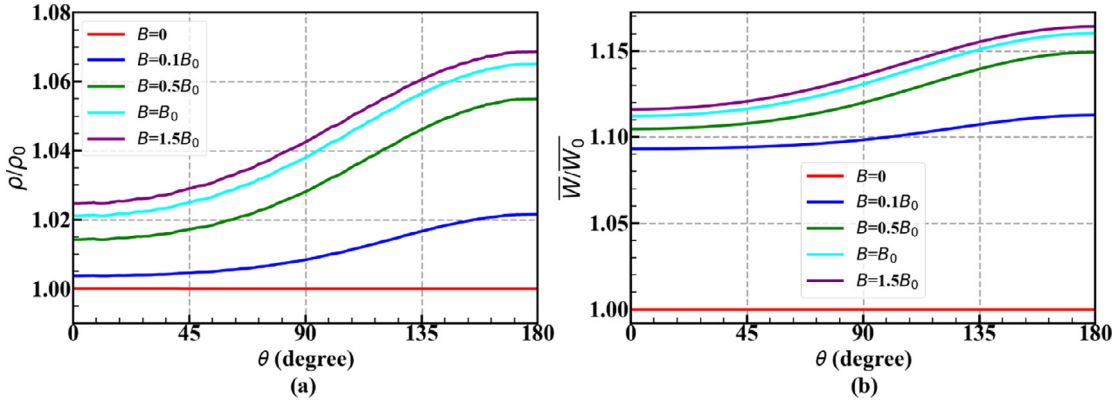

Fig. 7. Normalized density and molar mass distribution along the particle surface($T_{particle}$ = 1500 K, D_p = 400 μm, Re = 5, normalized by the density and molar mass of the incoming flow).

profiles around the particles, as shown in Fig. 7. The molar mass of the gas phase increases at the back side of the particle, which accounts for the increase of the pressure drop.

Meanwhile, Fig. 4(b) shows that the local drag due to friction is slightly different from the non-reactive particle at the front and rear of the particle, but the friction at the side of the particle is almost the same. For $0 < \theta < 30^\circ$, the friction force of a reactive particle is higher than that of a non-reactive particle. To explore the underlying physics, the kinematic viscosity distribution normalized by the parameter of the incoming flow is shown in Fig. 8. It is found that the kinematic viscosity in the boundary layer around the particle is lower than that of the incoming flow and the kinematic viscosity decreases with the increase of the surface angle of the cylinder. This is related to the species change around the particle, especially the accumulation of CO_2 at the rear of the particle. As the viscosity around the reactive particle is lower for $0 < \theta < 30^\circ$, the velocity gradient must be higher. Actually, because the streamwise velocity component of the Stefan flow in this region is opposite to the incoming flow, the velocity gradient will definitely be higher. For similar reason, in the region of $150^\circ < \theta < 180^\circ$, the reactive particle has a lower velocity gradient, so the friction is lower. Meanwhile, as Fig. 9 shows, the oxidation of CO causes a high temperature region around the particle, and therefore the kinematic viscosity coefficient increases. As a result, the velocity distribution is also different from that of a particle with pure Stefan flow, which influences the friction at the surface too. In addition, it is interesting to find that the normalized temperature and kinematic viscosity peak at around a location with a distance of D_p from the cylinder, in which gaseous reaction happens.

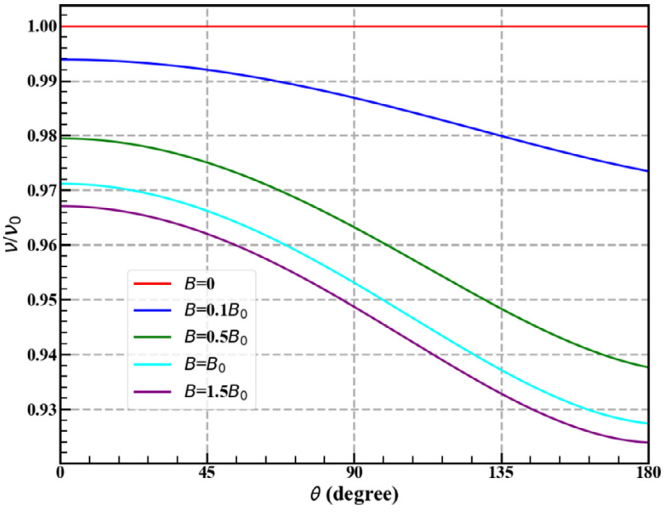

Fig. 8. Kinematic viscosity coefficient distribution around a particle with different reaction rates normalized by the viscosity at the inlet ($T_{particle}$ = 1500 K, D_p = 400 μm, Re = 5).

In many previous studies on the drag force of particle with outflow [13,14], Re_{stefan} is used as the only variable to describe the change in the drag force. However, when the gaseous reaction is introduced into the system, the situation becomes more complicated. Fig. 10 shows the correlations between the drag force coefficient and other variables. The symbol represents the simulation results, while the solid lines are obtained using quadratic polynomial fitting. When the Reynolds number and particle diameter are fixed,

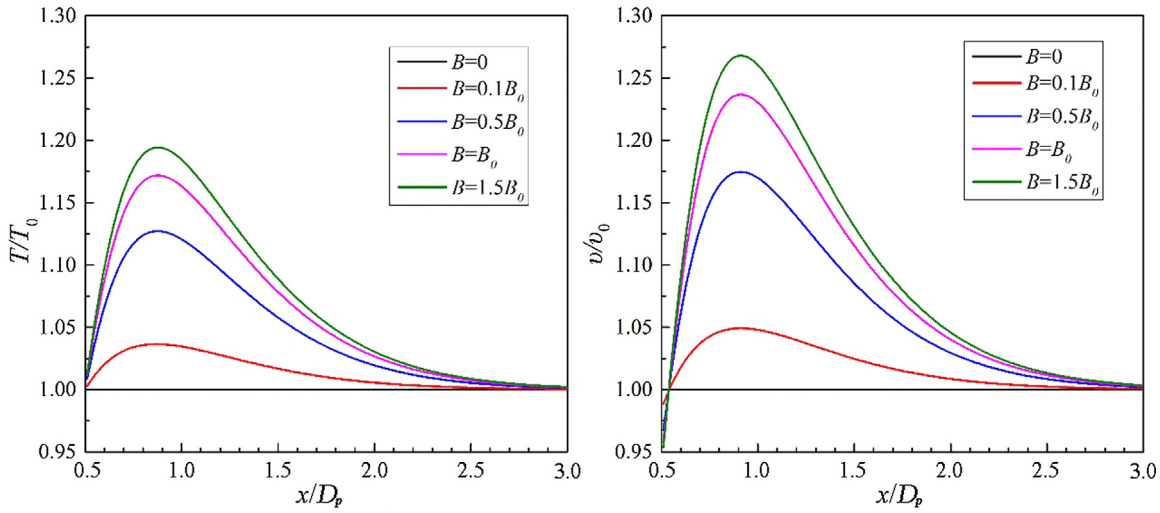

Fig. 9. Normalized temperature and kinematic viscosity coefficient (normalized by the values at the inlet) distribution as a function of normalized radial distance from the particle surface at $\theta = 90°$ ($T_{particle} = 1500$ K, $D_p = 400$ μm, $Re = 5$).

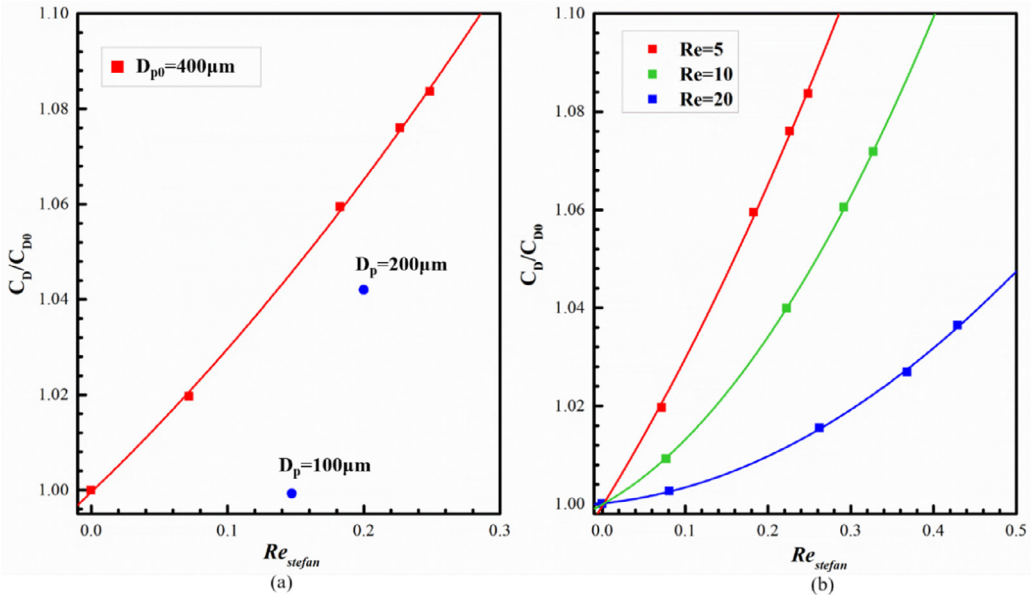

Fig. 10. Correlations between drag force coefficient and other variables (a) Variation of drag force coefficient with particle diameter and the Stefan flow Reynolds number when $Re = 5$ (b) Variation of drag force coefficient with the Reynolds number and the Stefan flow Reynolds number when $D_p = 400$ μm. (normalized by the drag force of the inert particle at the same Reynolds number).

the drag force has a quadratic dependence on Re_{stefan}. However, when the diameter of the particle is changed, Re_{stefan} is no longer enough to describe the drag force, as demonstrated in Fig. 10(a). In addition, it is found that the drag force of the reactive particle with D_p=100 μm is almost equal to that of the non-reactive particle (Re_{stefan}=0), indicating that the heterogeneous and gaseous reactions can even be neglected when the diameter is relatively small. The reason is that when the diameter becomes smaller, the time scales of convection $\tau_{conv} = D_p/U$ and diffusion $\tau_{\mathrm{diff}} = D_p^2/D_{\mathrm{CO}}$ both decrease so that the accumulation of products at the rear of the particle is attenuated. Fig. 10(b) confirms that when the particle diameter of 400 μm is fixed, the drag force coefficient correlates well with the Reynolds number and the Stefan flow Reynolds number. The drag force coefficent increases with the Stefan flow Reynolds number, but decreases with the Reynolds number when the Stefan flow Reynolds number is fixed. This also suggests that the effect of chemical reactions can be weakened by the convection. Fig. 11 presents the contours of Y_{CO} in the neighborhood of the particle with different diameters at the same Reynolds number. It is clear that the species of CO shows different profiles around the particle. For the particle with a larger diameter, CO is burnt at the surface, and the concentration is lower. The smaller particle shows higher char consumption rate, but CO tends to be transported and burnt far from the particle because of the stronger convection. These results suggest that besides the Reynolds number and the Stefan flow Reynolds number, other parameters related to gaseous reaction also influence the drag force of a burning particle.

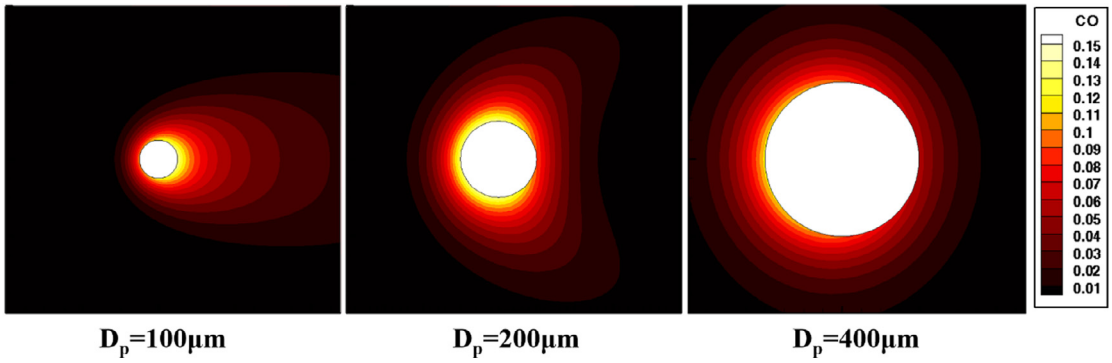

Fig. 11. Y_{CO} contours in the neighborhood of the particle with different diameters ($T_{particle}$ = 1500 K, Re = 5, $B = B_0$).

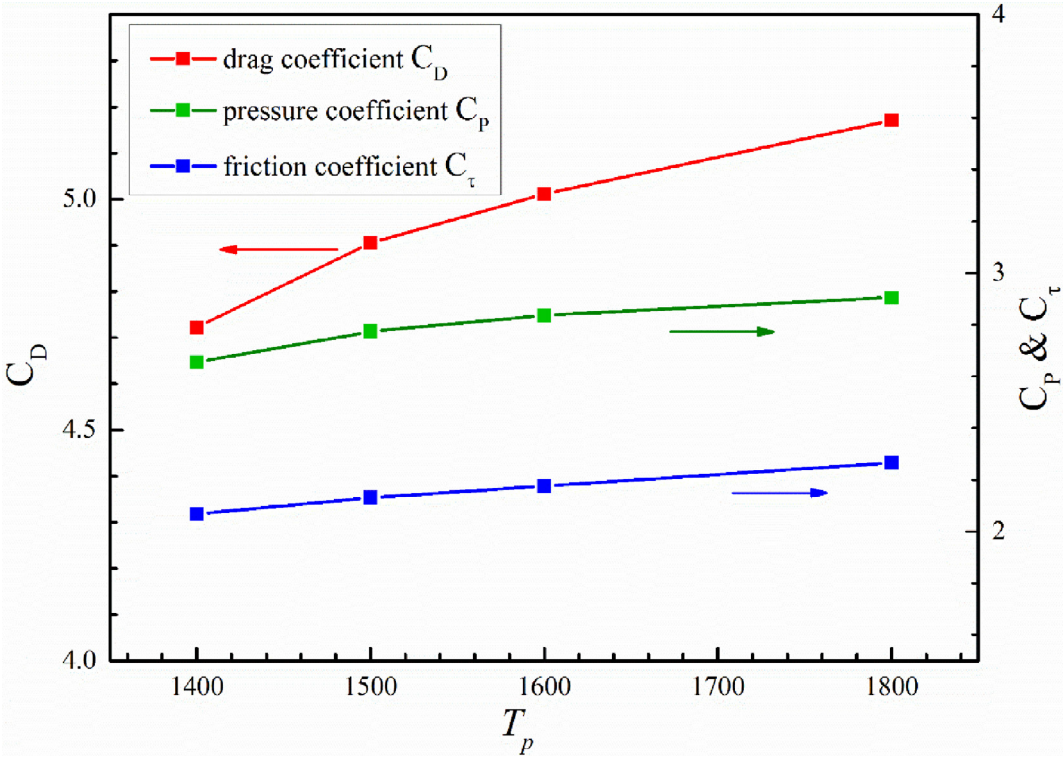

Fig. 12. Variation of drag force coefficient of a reactive particles with temperature (D_p = 400 μm, Re = 5, $B = B_0$).

3.3. Effect of the particle temperature

When the particle temperature is different from the incoming flow, the change of fluid properties must be taken into account. According to the study of Kurose et al. [20], the main factor of influence is the viscosity. While when a reactive particle has a different temperature from the temperature of the incoming flow, not only the viscosity, but also the reaction rates are affected, leading to different characteristics from the heated/cooled non-reactive particle. This effect will be discussed in this section.

Four cases are simulated and the results are presented in Fig. 12. The incoming flow temperature is fixed (1500 K), and the temperatures of reactive particles are 1400 K, 1500 K, 1600 K, and 1800 K, respectively. With the increase of the particle temperature, chemical reactions are expected to be more intense. It can be seen that both the pressure and friction terms linearly increase with the enhancement of the particle temperature. As for local distribution, it was found that the pressure of the heated particle is higher than that of the adiabatic particle in the region of $54^\circ < \theta < 108^\circ$, while lower at the rear of the particle in the study of Kurose et al. [20]. The reason was attributed to the shift of the separation point. But for a reactive particle here, the effect of separation point is eliminated by the Stefan flow. As a result, this phenomenon could not be observed any more as shown in Fig. 13(a). The higher particle temperature leads to larger pressure drop at the wake region of the particle, similar to Fig. 4(a). For the friction distribution, it is interesting to note that the friction peaks around θ=70° and the particle of higher temperature shows larger peak. This indicates that the stronger chemical reactions enhance the velocity gradient there as the kinematic viscosity is not obviously changed (Fig. 14).

3.4. Drag force correlation for a burning particle

According to the analysis above, reactions cause a difference in species and temperature distributions around a burning particle, leading to a shift of drag force. To take this effect into consideration, new drag force correlation needs to be developed.

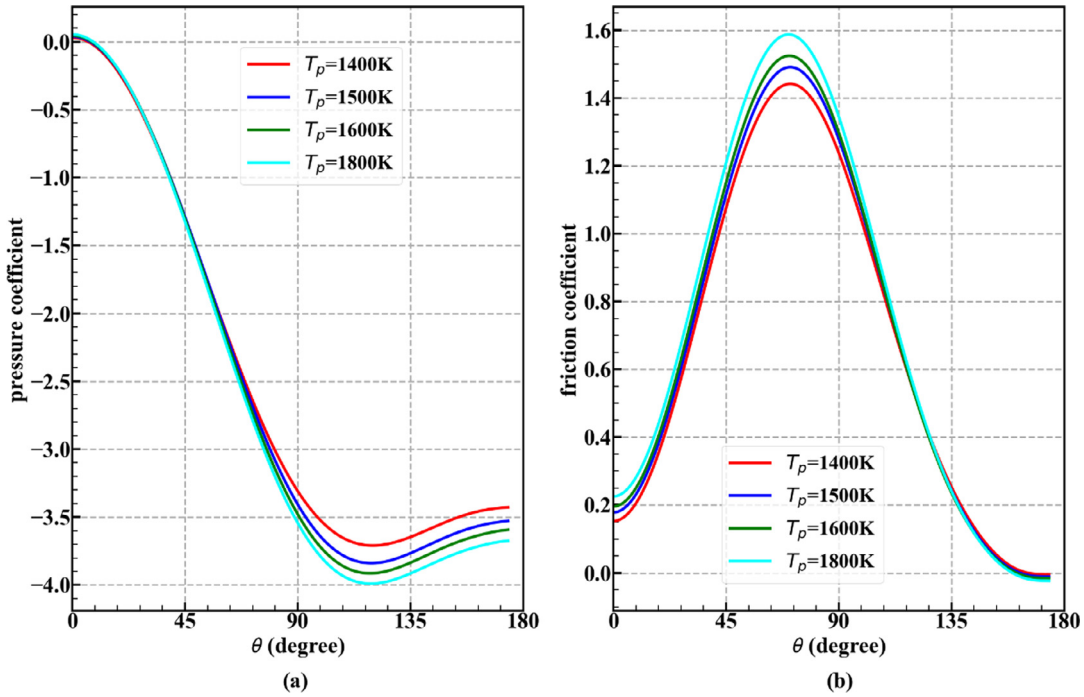

Fig. 13. Local pressure and friction coefficient distribution of particle with different temperatures (D_p = 400 μm, Re = 5, $B = B_0$).

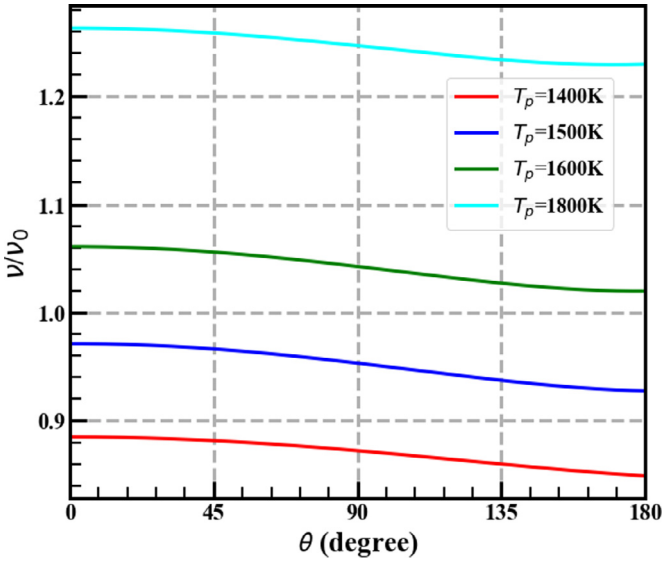

Fig. 14. Kinematic viscosity coefficient distribution around the particle with different temperatures (D_p = 400 μm, Re = 5, $B = B_0$).

For a burning char particle, besides the convection, the heat and mass transfer at the solid-fluid interface is related to three other processes, namely the heterogeneous reactions, the gaseous reaction and the diffusion. The effect of heterogeneous reactions is represented by the average char consumption rate on the surface, and the effect of gaseous reaction is described by using the reaction rate CO since only one gaseous reaction is involved in the present study. The process of diffusion is represented by the diffusion coefficient. According to the Buckingham π theorem [43], three more dimensionless variables can be deduced besides the Reynolds number and the temperature ratio. The temperature ratio is usually close to unity when char of pulverized coal particle burns in furnace. As a result, the average Stefan flow Reynolds number, the dimensionless gaseous reaction rate, and the diffusion Damköhler number are of relevance and can be expressed as follows

$$Re_{stefan} = \frac{\dot{m}_c D_p}{\rho \upsilon},\ m^*_{CO} = \frac{\dot{m}_{CO} D_p}{\rho U},\ Da_{diff} = \frac{\rho D_{CO}}{D_p^2 \dot{m}_{CO}}, \tag{16}$$

where ρ, U, υ are the density, streamwise velocity, and kinematic viscosity of the incoming flow, respectively. The char consumption rate is given by $\dot{m}_c$, while $\dot{m}_{CO}$ is the CO reaction rate of the gaseous reaction at the boundary of the particle. For point-particle based simulations [46–48], the char consumption rate can be obtained by using a char combustion model, such as the single-film model [49] or the double-film model [50]. As the present work focuses on the effect of chemical reactions on the drag force, the diffusion Damköhler number will not be discussed in the next analysis.

For a cylindrical particle, the drag force coefficient has been measured for cold flows in previous studies. Here to show the performance of the code, the drag force coefficient of a cold inert cylindrical particle is calculated from the current particle-resolved simulations and compared with the experimental data of Tritton [1]. As show in Fig. 15, the predicted drag force coefficient agrees well with the experimental data. Non-linear least square fitting is further used to obtain the following correlation:

$$C_D = \frac{24}{Re}\left(0.382 + 0.191 Re^{0.678}\right). \tag{17}$$

To consider the effect of chemical reactions, the average Stefan flow Reynolds number and the dimensionless gaseous reaction rate should be formulated into the correlation. From Fig. 10, it can be seen that C_D shows an approximately quadric dependence on Re_{stefan}. Assuming the similar quadratic behavior of $\dot{m}_{co}$, the correction for a burning particle can be formulated as below based

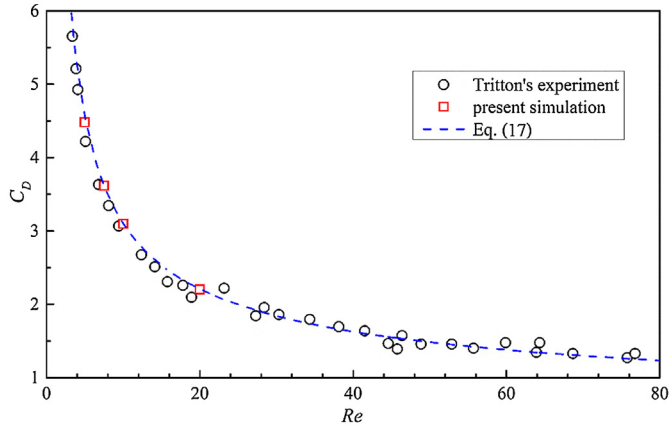

Fig. 15. Comparison of simulation data, experimental data [1], and Eq. (17).

on Eq. (17)

$$C_D = \frac{24}{Re}\Big[\left(0.382 + 0.191Re^{0.678}\right) + \left(a_1 Re_{stefan}^2 + b_1 m_{CO}^{*2} + c_1 Re_{stefan} m_{CO}^* + d_1 Re_{stefan} + e_1 m_{CO}^*\right) + \left(a_2 Re_{stefan}^2 + b_2 m_{CO}^{*2} + c_2 Re_{stefan} m_{CO}^* + d_2 Re_{stefan} + e_2 m_{CO}^*\right) Re^{0.678}\Big]. \quad (18)$$

For a cold non-reactive particle, both Re_{stefan} and m_{CO}^* are 0, and the above equation is reduced to Eq. (17). To determine the constants in the above equation, non-linear least squares fitting of the particle-resolved results is performed. Finally, the correlation becomes

$$C_D = \frac{24}{Re}\Big[\left(0.382 + 0.191Re^{0.678}\right) + \left(1.373 Re_{stefan}^2 + 16.715 m_{CO}^{*2} + 6.303 Re_{stefan} m_{CO}^* - 0.215 Re_{stefan} + 1.129 m_{CO}^*\right) - \left(0.144 Re_{stefan}^2 + 26.530 m_{CO}^{*2} - 1.288 Re_{stefan} m_{CO}^* - 0.315 m_{CO}^*\right) Re^{0.678}\Big]. \quad (19)$$

Fig. 16 shows the comparison of the drag force coefficient between the particle-resolved simulations and the fitted correlation at the Reynolds numbers of 5 and 10. The adjusted coefficient of determination R^2 [44] of this correlation is 0.99. For all cases used for fitting, the maximum error occurs at $Re = 5$ with a value of 0.3%.

To validate the correlation, a posteriori analysis is performed and presented in Fig. 17. Five additional cases at the Reynolds number of 7.5 are used. Parameters of these cases are shown in Table 3, including different reaction rates and diameters. Results show that these posterior cases are also in good agreement with the correlation. The maximum error is about 1.5%, which occurs at $D_p = 200$ μm.

Table 3
Parameters of posterior cases.

Case	Re	D_p (μm)	Pre-exponential factor
1	7.5	200	B_0
2	7.5	400	0
3	7.5	400	$0.5B_0$
4	7.5	400	$1.0B_0$
5	7.5	400	$1.5B_0$

For a cylinder with other orientation, or for a spherical particle, the effect of chemical reactions on the drag force is expected to show similar trends, but the correlation formula will be different because the reaction rates and species distributions will be different for different geometries. Nevertheless, the dimensionless numbers may remain to be the same, which lays a solid foundation for future study. This developed correlation can easily be coupled with point-source based simulations. All parameters required to calculate these dimensionless numbers can be obtained from the classic char combustion models [49,50]. The application and performance evaluation of this new drag force model for a burning particle needs further study in the future.

4. Conclusions

Particle-resolved simulations are performed to analyze the effect of chemical reactions on the drag force of a burning char particle by using the ghost cell immersed boundary method. The effects of heterogeneous reactions, gaseous reactions and the particle temperature are investigated. It is found that the flow patterns are changed due to the Stefan flow induced by the heterogeneous reactions. The recirculation wake becomes shorter and detaches from the particle, which leads to the change of the pressure, friction and drag force. As a result, the reactive particle can not be simplified as a particle with an outflow. The drag force of the reactive particle is obviously higher than the one with an outflow. The gaseous reaction of CO and O_2 also increases the drag force. The CO_2 produced by the gaseous reaction accumulates at the rear of

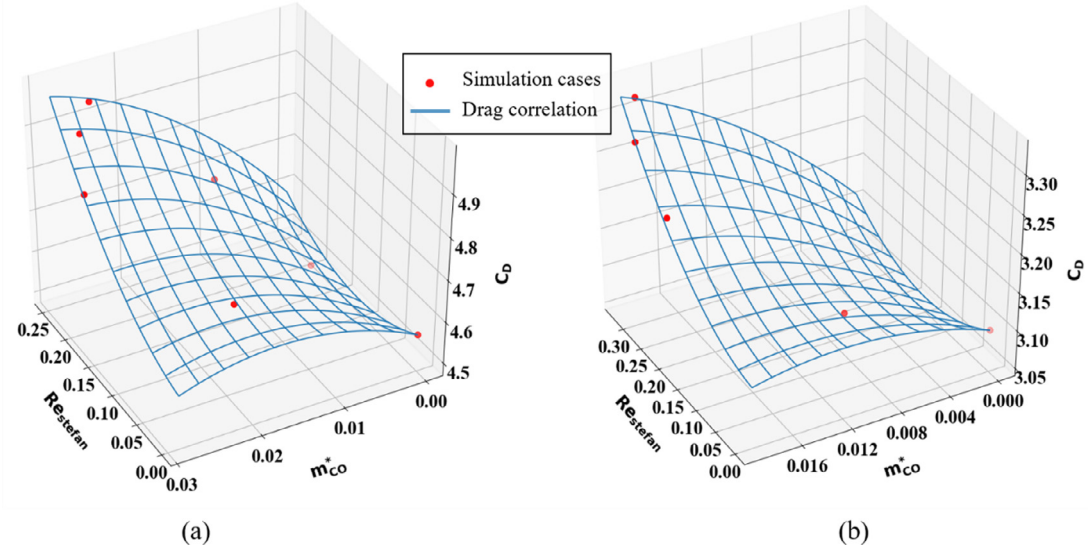

Fig. 16. Comparison of drag force coefficient between fully-resolved simulations and the fitted formulation (a) $Re = 5$, (b) $Re = 10$.

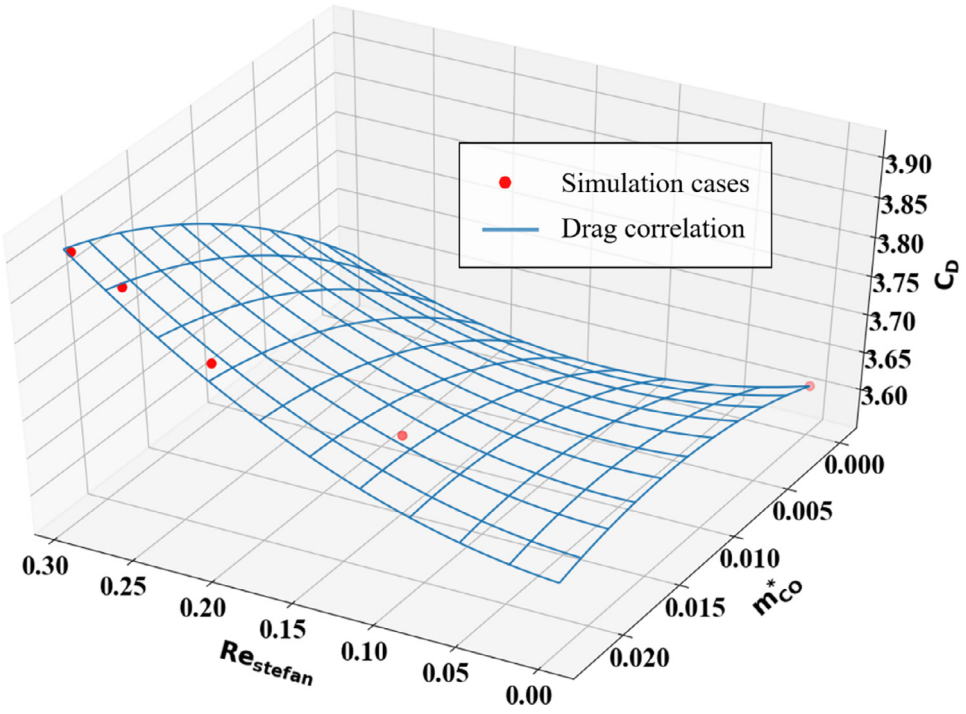

Fig. 17. Comparison of posterior analysis cases and predicted drag force.

the particle and causes a increase of the molar mass, leading to a larger pressure drop. Besides, the drag force is also influenced by the temperature difference between the particle and the incoming flow, not only through the viscosity but also through the chemical reactions. Based on the fully-resolved simulations, a new drag force correlation for a burning particle is developed. Two dimensionless numbers are introduced to represent the effects of the heterogeneous reactions and the gaseous reaction respectively. The correlation shows good performance in the current configurations, and need more evaluation in the future work.

Declaration of Competing Interest

The authors have no conflicts of interest to declare.

Acknowledgments

This work was financially supported by the National Key Research and Development Program of China (Nos. 2017YFB0601805 and 2017YFE0112500) and the European Union's Horizon 2020 Research and Innovation Program (No. 764697). We are grateful to that.

References

[1] D.J. Tritton, Experiments on the flow past a circular cylinder at low Reynolds numbers, J. Fluid Mech. 6 (1959) 547–567.
[2] S. Dennis, G.-.Z. Chang, Numerical solutions for steady flow past a circular cylinder at Reynolds numbers up to 100, J. Fluid Mech. 42 (1970) 471–489.
[3] R. Clift, J. Grace, M. Weber, Bubbles, drops, and particles, Academic Press, New York, 1978, p. 510.
[4] T.J. Poinsot, S.K. Lelef, A drag coefficient correlation, 1933 Ver. Deut. Ing., 77 318–320.
[5] T. Hara, M. Muto, T. Kitano, R. Kurose, S. Komori, Direct numerical simulation of a pulverized coal jet flame employing a global volatile matter reaction scheme based on detailed reaction mechanism, Combust. Flame 162 (2015) 4391–4407.
[6] M. Rieth, A. Kempf, A. Kronenburg, O. Stein, Carrier-phase DNS of pulverized coal particle ignition and volatile burning in a turbulent mixing layer, Fuel 212 (2018) 364–374.
[7] T. Brosh, D. Patel, D. Wacks, N. Chakraborty, Numerical investigation of localised forced ignition of pulverised coal particle-laden mixtures: a direct numerical simulation (DNS) analysis, Fuel 145 (2015) 50–62.
[8] P. Nithiarasu, K. Seetharamu, T. Sundararajan, Natural convective heat transfer in a fluid saturated variable porosity medium, Int. J. Heat Mass Transf. 40 (1997) 3955–3967.
[9] L. Leal, A. Acrivos, The effect of base bleed on the steady separated flow past bluff objects, J. Fluid Mech. 39 (1969) 735–752.
[10] S. Bhattacharyya, S. Dhinakaran, A. Khalili, Fluid motion around and through a porous cylinder, Chem. Eng. Sci. 61 (2006) 4451–4461.
[11] S. Yu, P. Yu, T. Tang, Effect of thermal buoyancy on flow and heat transfer around a permeable circular cylinder with internal heat generation, Int. J. Heat Mass Transf. 126 (2018) 1143–1163.
[12] K. Wittig, P. Nikrityuk, A. Richter, Drag coefficient and Nusselt number for porous particles under laminar flow conditions, Int. J. Heat Mass Transf. 112 (2017) 1005–1016.
[13] M. Watanabe, J. Yahagi, Effects of nonuniform outflow and buoyancy on drag coefficient acting on a spherical particle, J. Flow Control Meas. Vis. 5 (2017) 99.
[14] R. Kurose, H. Makino, S. Komori, M. Nakamura, F. Akamatsu, M. Katsuki, Effects of outflow from the surface of a sphere on drag, shear lift, and scalar diffusion, Phys. Fluids 15 (2003) 2338–2351.
[15] T. Jayawickrama, N. Haugen, M. Babler, K. Umeki, Effect of Stefan flow on drag coefficient of reactive spherical particles in gas flow, ICHMT Digital Library Online, Begel House Inc, 2018.
[16] M. Stöllinger, B. Naud, D. Roekaerts, N. Beishuizen, S. Heinz, PDF modeling and simulations of pulverized coal combustion–part 1: theory and modeling, Combust. Flame 160 (2013) 384–395.
[17] T.R. Jayawickrama, N.E.L. Haugen, M.U. Babler, M.A. Chishty, K. Umeki, The effect of Stefan flow on the drag coefficient of spherical particles in a gas flow, Int. J. Multiph. Flow 117 (2019) 130–137.
[18] F. Higuera, Combustion of a coal char particle in a stream of dry gas, Combust. Flame 152 (2008) 230–244.
[19] K. Luo, C. Mao, J. Fan, Z. Zhuang, N.E.L. Haugen, Fully resolved simulations of single char particle combustion using a ghost-cell immersed boundary method, AIChE J. 64 (2018) 2851–2863.
[20] R. Kurose, M. Anami, A. Fujita, S. Komori, Numerical simulation of flow past a heated/cooled sphere, J. Fluid Mech. 692 (2012) 332–346.
[21] T. Nagata, T. Nonomura, S. Takahashi, Y. Mizuno, K. Fukuda, Direct numerical simulation of flow around a heated/cooled isolated sphere up to a Reynolds number of 300 under subsonic to supersonic conditions, Int. J. Heat Mass Transf. 120 (2018) 284–299.
[22] C.R. Shaddix, E.S. Hecht, C. Gonzalo-Tirado, B.S. Haynes, The effect of bulk gas diffusivity on apparent pulverized coal char combustion kinetics, Proc. Combust. Inst. 37 (2019) 3071–3079.
[23] N.E.L. Haugen, J. Krüger, D. Mitra, T. Løvås, The effect of turbulence on mass transfer rates of small inertial particles with surface reactions, J. Fluid Mech. 836 (2018) 932–951.

[24] S. Farazi, M. Sadr, S. Kang, M. Schiemann, N. Vorobiev, V. Scherer, H. Pitsch, Resolved simulations of single char particle combustion in a laminar flow field, Fuel 201 (2017) 15–28.
[25] M. Renksizbulut, M. Yuen, Experimental study of droplet evaporation in a high-temperature air stream, J. Heat Transf. 105 (1983) 384–388.
[26] R.S. Miller, J. Bellan, Direct numerical simulation of a confined three-dimensional gas mixing layer with one evaporating hydrocarbon-droplet-laden stream, J. Fluid Mech. 384 (1999) 293–338.
[27] A. Brandenburg, W. Dobler, Pencil: finite-difference code for compressible hydrodynamic flows, astrophysics source code library, (2010).
[28] N. Babkovskaia, N. Haugen, A. Brandenburg, A high-order public domain code for direct numerical simulations of turbulent combustion, J. Comput. Phys. 230 (2011) 1–12.
[29] G. Lupo, M.N. Ardekani, L. Brandt, C. Duwig, An immersed boundary method for flows with evaporating droplets, Int. J. Heat Mass Transf. 143 (2019) 118563.
[30] K. Luo, Z. Zhuang, J. Fan, N.E.L. Haugen, A ghost-cell immersed boundary method for simulations of heat transfer in compressible flows under different boundary conditions, Int. J. Heat Mass Transf. 92 (2016) 708–717.
[31] L. Zhang, K. Liu, C. You, Fictitious domain method for fully resolved reacting gas–solid flow simulation, J. Comput. Phys. 299 (2015) 215–228.
[32] S.R. Turns, An introduction to combustion, McGraw-Hill, New York, 1996.
[33] S. Sundaresan, N.R. Amundson, Diffusion and reaction in a stagnant boundary layer about a carbon particle. 6. Effect of water vapor on the pseudo-steady-state structure, Ind. Eng. Chem. Fundam. 19 (1980) 351–357.
[34] S. Tenneti, R. Garg, S. Subramaniam, Drag law for monodisperse gas–solid systems using particle-resolved direct numerical simulation of flow past fixed assemblies of spheres, Int. J. Multiph. Flow 37 (2011) 1072–1092.
[35] R.J. Hill, D.L. Koch, A.J. Ladd, The first effects of fluid inertia on flows in ordered and random arrays of spheres, J. Fluid Mech. 448 (2001) 213–241.
[36] R.J. Hill, D.L. Koch, A.J. Ladd, Moderate-Reynolds-number flows in ordered and random arrays of spheres, J. Fluid Mech. 448 (2001) 243–278.
[37] M.A. van der, Hoef, R. Beetstra, J. Kuipers, Lattice-Boltzmann simulations of low-Reynolds-number flow past mono-and bidisperse arrays of spheres: results for the permeability and drag force, J. Fluid Mech. 528 (2005) 233–254.
[38] C. Wilke, A viscosity equation for gas mixtures, J. Chem. Phys. 18 (1950) 517–519.
[39] W. Sutherland, LII. The viscosity of gases and molecular force, Lond. Edinb. Dublin Philos. Mag. J. Sci. 36 (1893) 507–531.
[40] P. Yu, Y. Zeng, T. Lee, H. Bai, H. Low, Wake structure for flow past and through a porous square cylinder, Int. J. Heat Fluid Flow 31 (2010) 141–153.
[41] P. Yu, Y. Zeng, T.S. Lee, X.B. Chen, H.T. Low, Steady flow around and through a permeable circular cylinder, Comput. Fluids 42 (2011) 1–12.
[42] M. Renksizbulut, M. Yuen, Numerical study of droplet evaporation in a high--temperature stream, J. Heat Transf. 105 (1983) 389–397.
[43] E. Buckingham, On physically similar systems; illustrations of the use of dimensional equations, Phys. Rev. 4 (1914) 345.
[44] G. Shieh, Improved shrinkage estimation of squared multiple correlation coefficient and squared cross-validity coefficient, Organ. Res. Methods 11 (2008) 387–407.
[45] T.J. Poinsot, S.K. Lelef, Boundary conditions for direct simulations of compressible viscous flows, J. Comput. Phys. 101 (1) (1992) 104–129.
[46] Kun Luo, Yun Bai, Tai Jin, Kunzan Qiu, Jianren Fan, Direct numerical simulation study on the stabilization mechanism of a turbulent lifted pulverized coal jet flame in a heated coflow, Energy & Fuels 31 (8) (2017) 8742–8757.
[47] Masaya Muto, Kohei Yuasa, Ryoichi Kurose, Numerical simulation of ignition in pulverized coal combustion with detailed chemical reaction mechanism, Fuel 190 (2017) 136–144.
[48] M. Rieth, A.M. Kempf, A. Kronenburg, O.T. Stein, Carrier-phase DNS of pulverized coal particle ignition and volatile burning in a turbulent mixing layer, Fuel 212 (2018) 364–374.
[49] W.Z. Nusselt, The process of combustion in powdered coal firing, Ver Z Deut Ing 68 (1924) 124–128.
[50] H.S. Burke, T.E.W. Schumann, The mechanism of combustion of solid fuel, Proceedings of the International Conference on Bituminous Coal 2 (1932) 485.